Supporting Information

Quantum Confinement vs. Mesoporosity in SnO_2: Oxygen Vacancies Dictate Dominant Formate Selectivity in Hybrid CO_2 Electrolysis with Unprecedented 480 mV Energy Savings

*Souradip Ganguly,[a,b #] Pooja Basera,[c,d #] Kajari Dutta,[e] Sukanta Saha,[f] Arnab Dutta,[f] Ashish Sharma,[g] Govindasamy Jayamurugan,[g] Sahnawaz Ahmed,[h] Chanchal Loha [a] and Sirshendu Ghosh [a,i] **

[a]Energy Research & Technology Group, CSIR-Central Mechanical Engineering Research Institute, Durgapur-713209, West Bengal, India.

[b]Academy of Scientific and Innovative Research (AcSIR), Ghaziabad-201002, India.

[c]SUNCAT Center for Interface Science and Catalysis, Department of Chemical Engineering, Stanford University, Stanford, California 94305, United States.

[d]SUNCAT Center for Interface Science and Catalysis, SLAC National Accelerator Laboratory, Menlo Park, California 94025, United States.

[e]Department of Physics, Amity Institute of Applied Sciences, Amity University Kolkata, Kolkata, West Bengal, 700135, India.

[f]Department of Chemistry, Indian Institute of Technology Bombay, Mumbai 400076, India.

[g]Institute of Nano Science and Technology, Sector 81, Mohali, Punjab 140306, India.

[h]Department of Medicinal Chemistry, National Institute of Pharmaceutical Education and Research (NIPER) Kolkata, Kolkata 700054, India.

[i]School of Mathematics and Natural Sciences, Chanakya University, Bengaluru-562165, Karnataka, India.

[#]S. Ganguly and Dr. P. Basera contributed equally to this work.

*Corresponding Author Email: sirshendu.g@chanakyauniversity.edu.in

Chemicals

Stannic chloride pentahydrate ($SnCl_4.5H_2O$), Hydrazine hydrate ($NH_2NH_2.H_2O$), ethylene diamine – all were purchased from Sigma Aldrich. All chemicals were used as received without any further purification. Solvents viz. Iso-propyl alcohol (99%, synthesis) and Ethanol (CH_3CH_2OH) were purchased from Loba Chemie. Water used for cleaning the electrode and electrochemical measurement was De-ionised water.

Electrochemical characterisation

Ink & Working Electrode Preparation:

Catalyst inks for the electrochemical experiments were prepared by well dispersing the mixture of 1 mg of blended as-synthesized catalyst in 100 μL Nafion solution (from, 1 mL of isopropanol, 75 μL of 5% Nafion solution) followed by sonication for 30 mins. Working electrodes were prepared by drop-casting 100 μL of catalyst ink onto a conducting Carbon Cloth and were dried in room temperature overnight. Electrochemical experiments were performed in 1 M NaOH solution using the standard three-electrode system taking Ag/AgCl and graphite rod as a reference and counter electrode, respectively.

CO_2 electroreduction experiments were further conducted in a commercial GDE flow-cell configuration comprising separate compartments for the anolyte, catholyte, and gas phase. The anodic and cathodic chambers were isolated by a proton-exchange membrane (Nafion 117). CO_2 was continuously supplied to the system at a controlled rate using a mass flow controller, and electrolyte circulation in the cell was maintained by a peristaltic pump operating under steady-flow conditions.

Polarization curves were recorded on a CHI-600E instrument and analysed using the CHI – 600e program. All measurements were referred to the RHE using the relationship:

$\mathbf{E_{(RHE)} = E_{(Ag/AgCl)} + E^0_{(Ag/AgCl)} + 0.059V \times pH}$, where, $E^0_{(Ag/AgCl)}$ = + 0.197 **V**, at T = 25 °C.

All electrochemical measurements were repeated at least three times using independently prepared electrodes unless otherwise stated. Reported values correspond to the mean, and error bars represent the standard deviation of independent measurements.

Material Synthesis

Synthesis of SnO_2 nanoflower:

In the typical synthesis,[1] a 3 × 1.5 cm^2 tin (Sn) foil was initially treated with 0.1 N hydrochloric acid (HCl) for a few minutes to remove surface oxides and impurities. Subsequently, the foil underwent sequential sonication in acetone and ethanol to eliminate any remaining organic residues, followed by rinsing with deionized (DI) water and drying under a nitrogen stream. The pretreated Sn foil was then introduced into a 50 mL Teflon-lined stainless steel autoclave containing an aqueous solution of 0.01 N sodium hydroxide (NaOH), hydrazine hydrate ($NH_2NH_2{\cdot}H_2O$), and ethylenediamine in a molar ratio of 1:0.5:0.5. The autoclave was hermetically sealed and

maintained at 200 °C for 24 hours in a convection oven. Upon cooling to room temperature, the resultant product was collected via centrifugation, extensively washed with DI water, acetone, and ethanol to remove unreacted species and byproducts, and finally dried under vacuum overnight to yield the desired powder material.

Synthesis of SnO_2 quantum dots:

In the typical synthesis of SnO_2 quantum dots,[2] a total of 5.83 mmol of $SnCl_4 \cdot 5H_2O$ was dissolved in a solvent mixture composed of 18.5 mL ethanol and 9.28 mL ethylenediamine under continuous magnetic stirring for 1 hour. Following this, 58.32 mmol of urea—pre-dissolved in 18.5 mL of deionized (DI) water—was added to the reaction mixture and stirred further for an additional 30 minutes to ensure homogeneity. The resulting white suspension was then transferred into a 50 mL Teflon-lined stainless-steel autoclave and heated at 90 °C for 8 hours in a laboratory oven. Upon naturally cooling to ambient temperature, the solid product was isolated by centrifugation and thoroughly washed several times with DI water and ethanol to remove residual impurities. Finally, the obtained material was dried under vacuum overnight to yield the final powdered product.

Material Characterisations:

XRD: X-ray powder diffraction data spanning 20° to 80° were collected using an XRD Rigaku SmartLab diffractometer with Cu-Kα radiation (1.54Å).

TEM: UHR – FEG transmission electron microscope (TEM) was used for structural and morphology study of the nano-catalysts, including high-resolution TEM (HRTEM), high-angle annular dark-field scanning transmission electron microscopy (HAADF-STEM) and energy-dispersive spectra (EDS) for elemental mapping.

XPS: X-ray photoelectron spectroscopy (XPS), carried out using an Omicron instrument (model: 1712-62-11), utilized Al-Kα radiation source at 15 kV voltage and 5 mA current to discern the valence states of the constituents. The XPS data were further deconvoluted with XPSPEAK 41 software.

EPR: Bruker EMX Plus series instrument was used for the EPR (X – band and Q – band) study.

NMR: Brukner Advance-II (400 MHz) NMR instrument was used for detection of the electrocatalytically oxidised and reduced products. The products were quantified from known amount of tetramethyl ammonium chloride (TMACl) as an internal standard in D_2O. 500 µl of each of solution was mixed with 100 µl of 0.01 M solution of TMACl in D_2O.

GC: Thermo scientific trace 1000 GC instrument was used to analyse gases generated from water splitting.

Computational details

The first-principles calculations have been performed using Vienna Ab Initio Simulation Package[3] to study CO_2RR and HER on Sn based surfaces. Projector-augmented wave potentials were employed to replace the inner cores of the atoms with all-electron, frozen cores. The Perdew-Burke-Ernzerhof (PBE) exchange-correlation functional

was used to account for exchange and correlation effects[4]. The calculations were carried out on a Monkhorst-Pack grid centered around the Γ-point. The energy convergence threshold for the relaxation of energies was set to 10^{-5} eV, ensuring the accuracy of the results. Furthermore, atomic forces were converged to 0.01 eV/Å for stable atomic positions. We investigated the reaction energetics of CO_2RR and the competing hydrogen evolution reaction (HER) on Sn, SnO_2, SnO, SnO_2/SnO. For this, Sn (211), SnO (011), SnO_2(110) surface without and with an O-vacancy, SnO(011)/SnO_2(110) and SnO(001)/SnO_2(110) heterostructures were modeled with a slab of 4 atomic layers, in which the bottom two layers were frozen, and a vacuum layer of about 15 Å along the z-axis was built. The slabs were optimized using a 4 × 4 × 1 Monkhorst-Pack grid, with a cutoff energy set at 500 eV.

The reaction steps considered for the electrochemical reduction of CO_2 to formic acid, CO, and the competing HER are as follows:

1. **Formation of CO:**

   $CO_2 + * + H_2 \rightarrow *COOH + ½\ H_2$

   $*COOH + ½\ H_2 \rightarrow *CO + H_2O$

   $*CO + H_2O \rightarrow CO + * + H_2O$

2. **Formation of HCOOH:**

   $CO_2 + * + H_2 \rightarrow *OCHO \text{ or } HCOO* + ½\ H_2$

   $*OCHO + ½\ H_2 \rightarrow HCOOH + *$

3. **Hydrogen Evolution Reaction**:

   $2H^+ + 2e^- \rightarrow H_2$

The Gibbs free energies at 298.15 K and 1 atm for each step along the CO_2 RR and HER pathway were computed using equation:

$$G = H - TS = E_{DFT} + E_{ZPE} + \int_0^{298.15K} C_V dT - TS$$

To ensure accurate Gibbs free energy calculations, we included both zero-point energies (ZPE) and entropy corrections (TS). The ZPE and TS values aligned well with the previous reports[5, 6]. To address known inaccuracies in DFT, particularly the overbinding of O_2 and self-interaction errors, we applied a correction scheme where the DFT energy of O_2(g) is referenced to experimental formation enthalpy of water and hydrogen[7, 8]. The computational hydrogen electrode (CHE) model[9] was used to calculate the free energy of electrocatalytic CO_2RR.

Calculation of % product conversion of oxidation and reduction of the substrates:

6 ml electrolyte, undivided three electrode electrochemical cell (and H-type cell separated with Nafion 117 membrane for paired electrolysis), graphite rod as counter electrode, Ag/AgCl as reference electrode,1.0 mg catalyst deposited over 1×1 cm^2 carbon cloth.

The electrolyte solution after the chronoamperometry studies were analysed and quantified from ^{1}H and ^{13}C NMR spectroscopy using TMACl (Tetramethyl Ammonium chloride) as internal standard and D_2O as locking agent.

Product Analysis:

The % product conversion was calculated as follows:

500 µL of analyte + 100 µL of 0.1 M TMACl => Conc. of TMACl in the (600 µL) solution = 16.6 mM.

Now, TMACl consists of 12 H atom. Thus, the conc. of H ([H]) could be determined with respect to the integration of 1 equivalent TMACl corresponding to 12 H.

$\therefore$ [H] ≡ integration of ≡ 16.6 × 12 mM [H]

= 200 mM [H].

The Faradaic efficiency (FE) toward formate formation was calculated using the following equation:

$FE\ (\%) = (n \cdot z \cdot F / Q) \times 100$

Here, *n* is the quantity of formate produced (mol), *z* is the number of electrons transferred per mole of product (z = 3 for EGOR and z = 2 for CO_2RR), *Q* denotes the total charge consumed during electrolysis (C), and *F* is the Faraday constant (96,485 C mol^{-1}).

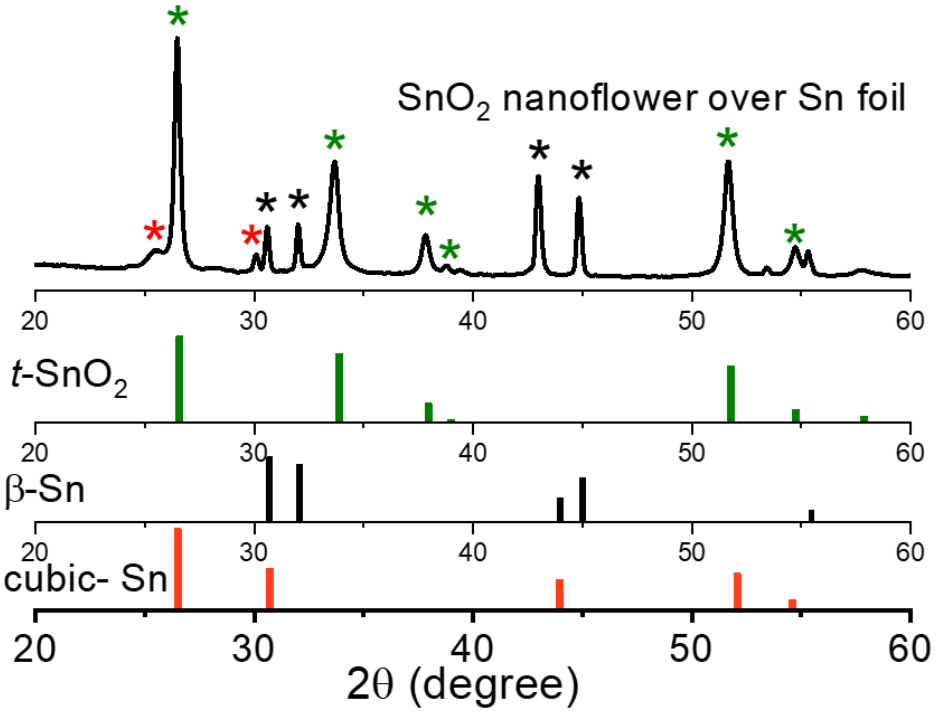

Fig. S1. XRD pattern of SnO_2 NF grown over Sn foil along with standard pattern for different phases of Sn and SnO_2.

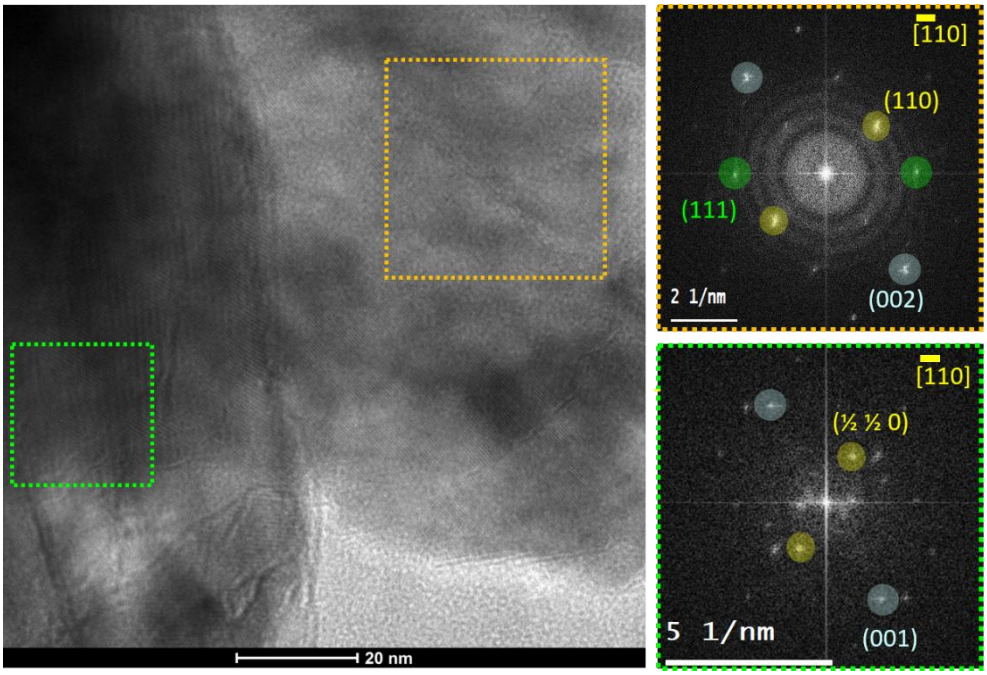

Fig. S2. HRTEM image and corresponding FFT patterns of two adjacent nano-petals showing single crystalline nature of each petal.

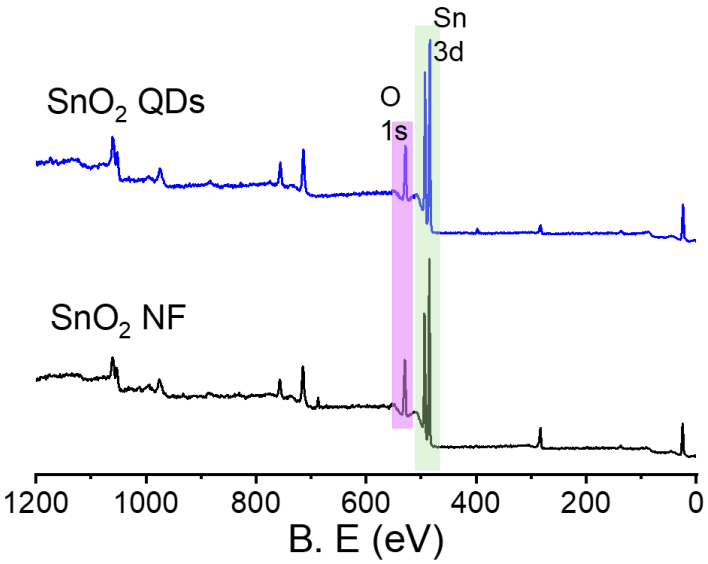

Fig. S3. Survey XPS spectra of SnO_2 QDs and NF.

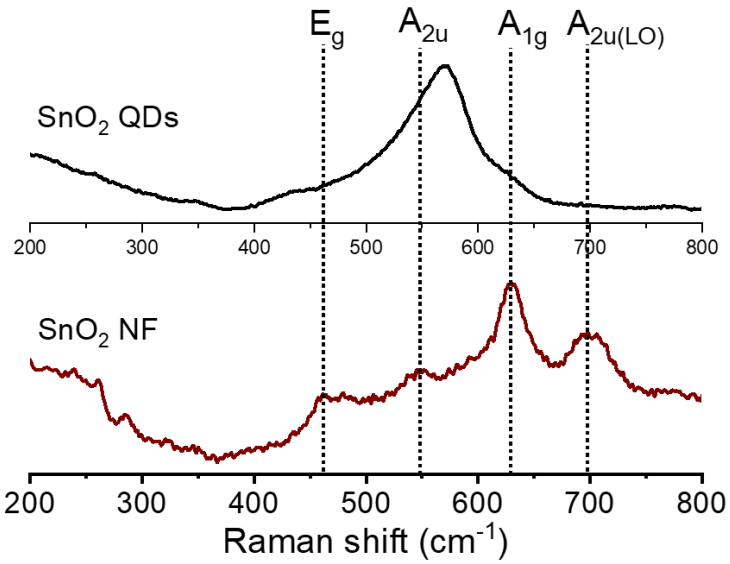

Fig. S4. Raman spectra of SnO_2 QDs and NF.

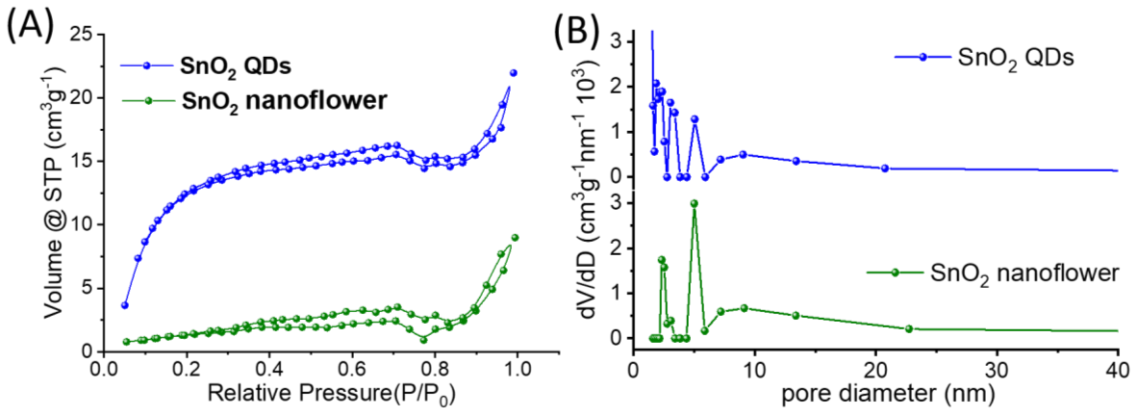

Fig. S5. (A) Nitrogen adsorption–desorption isotherms of NF and QDs at 77 K. (B) Pore size distributions of QDs and NF.

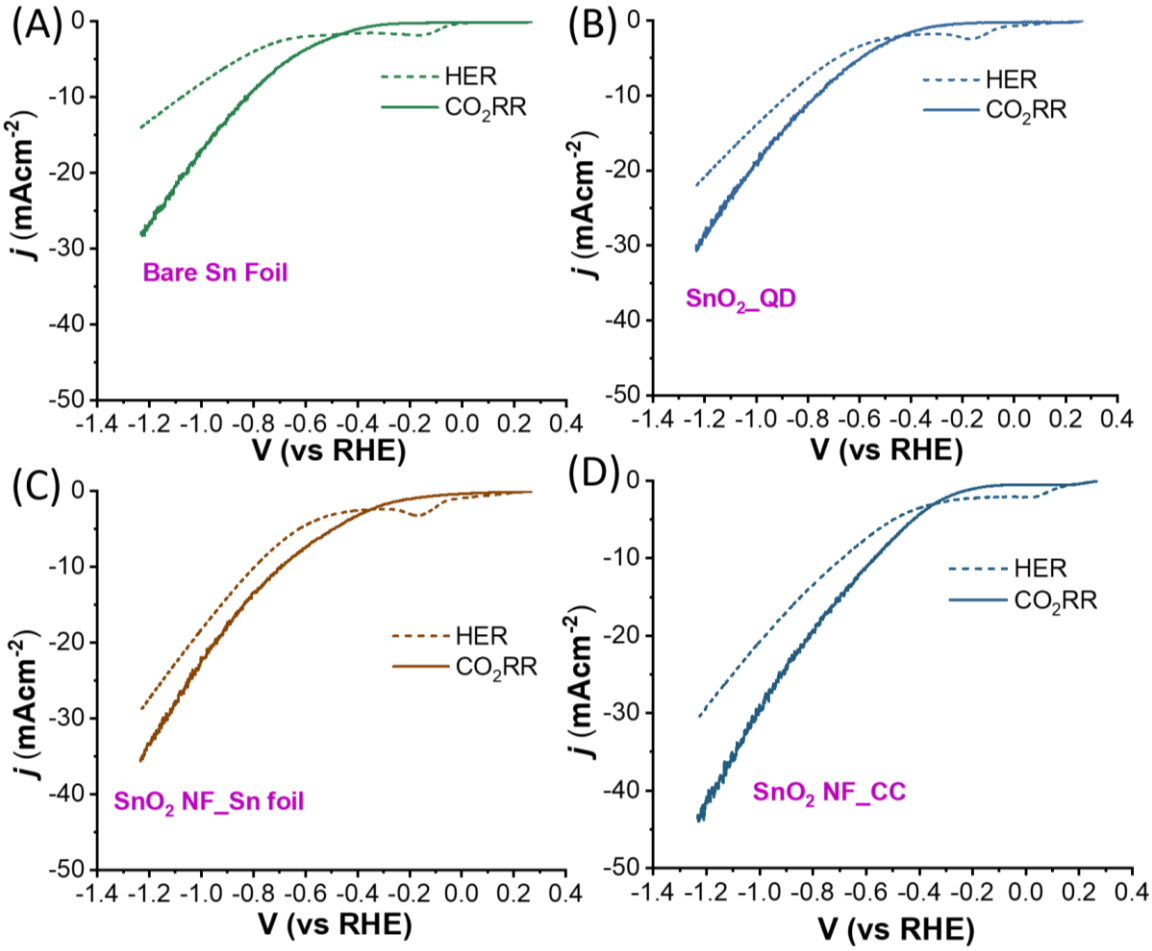

Fig. S6. LSV curves in Ar (HER) or CO_2-saturated 0.5 M $NaHCO_3$ at a scan rate of 10 mVs^{-1} for (A) bare Sn foil, (B) SnO_2 QDs, (C) SnO_2 NF over Sn foil and (D) SnO_2 NF over carbon cloth.

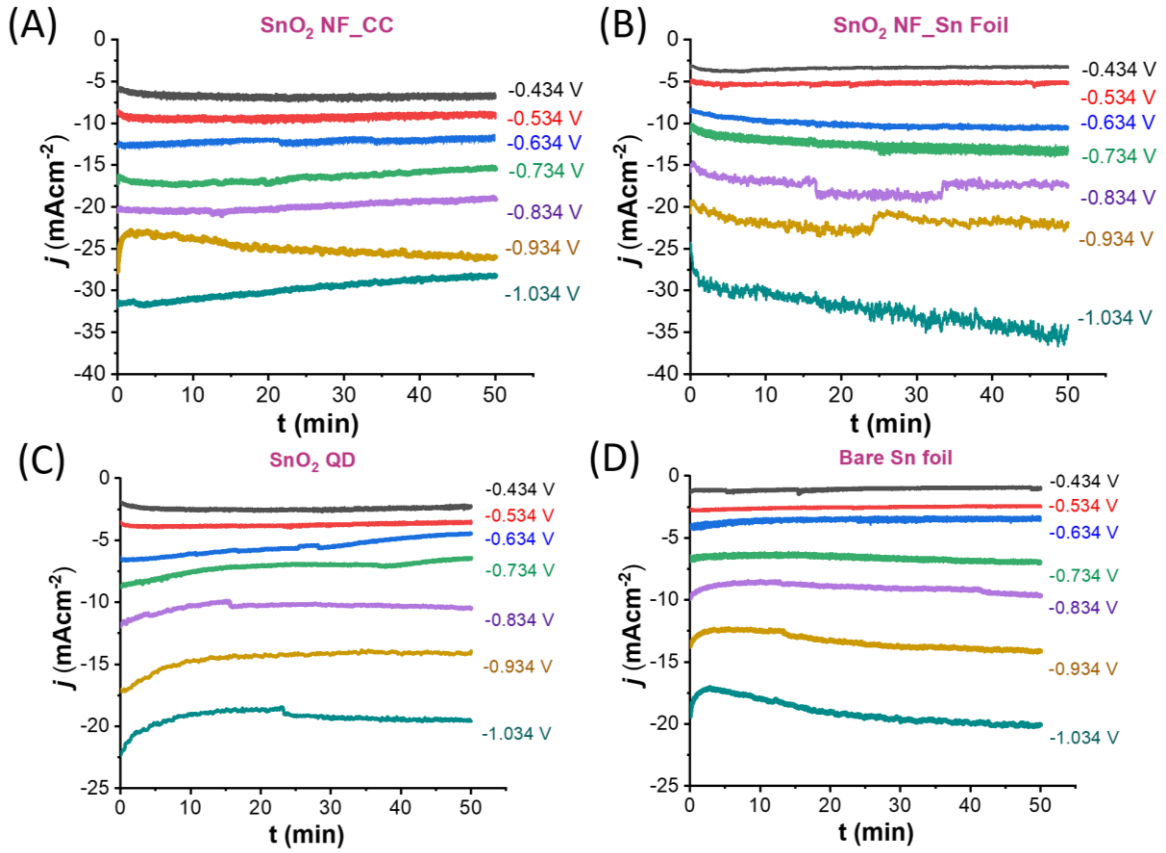

Fig. S7. Chronoamperometry studies of (A) SnO_2 NF deposited over CC, (B) SnO_2 NF grown over Sn foil, (C) SnO_2 QDs deposited over CC and (D) bare cleaned Sn -foil for CO_2RR at variable potentials.

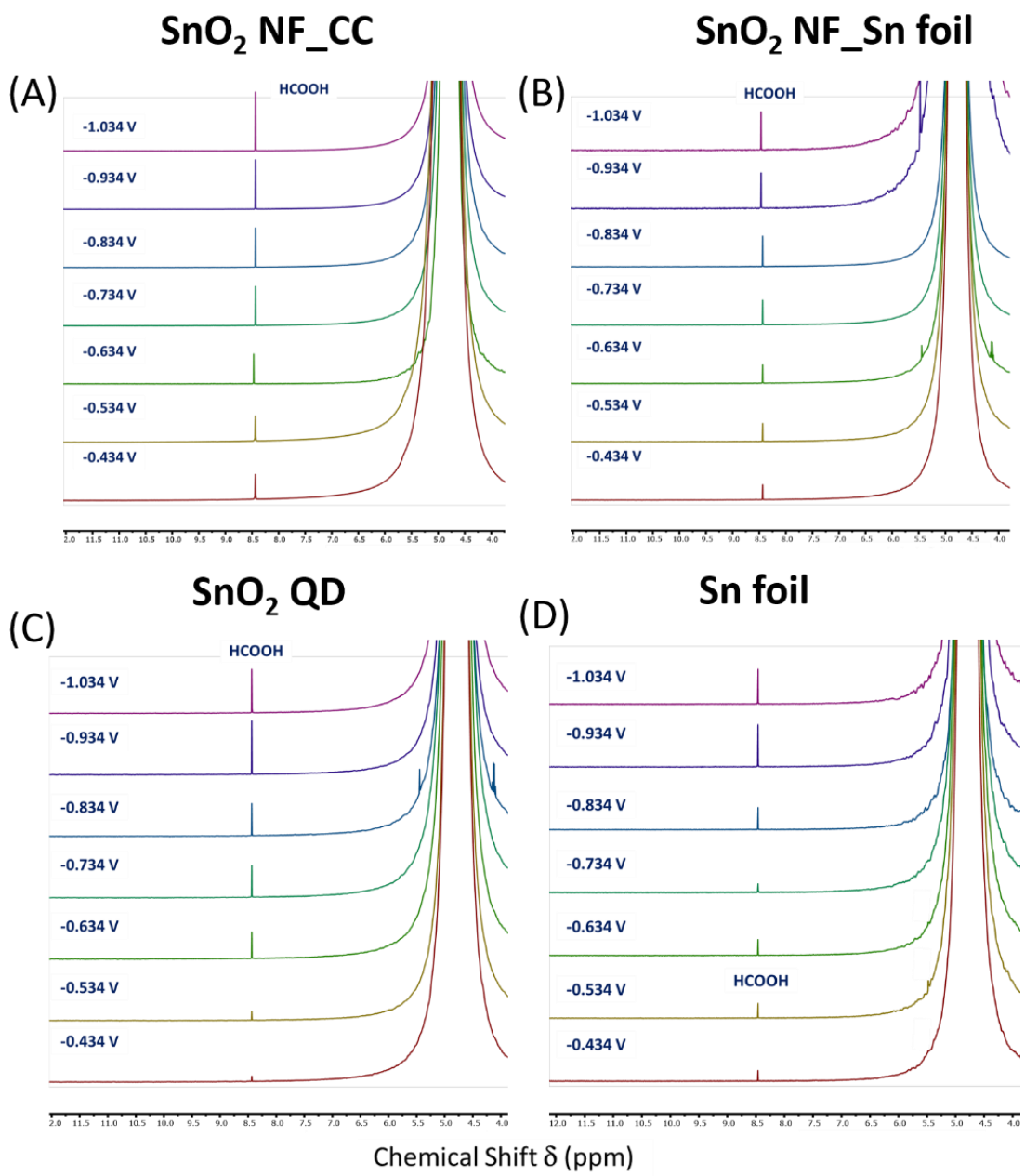

Fig. S8. ^{1}H NMR of products formed after chronoamperometry studies during CO_2RR with various electrocatalysts.

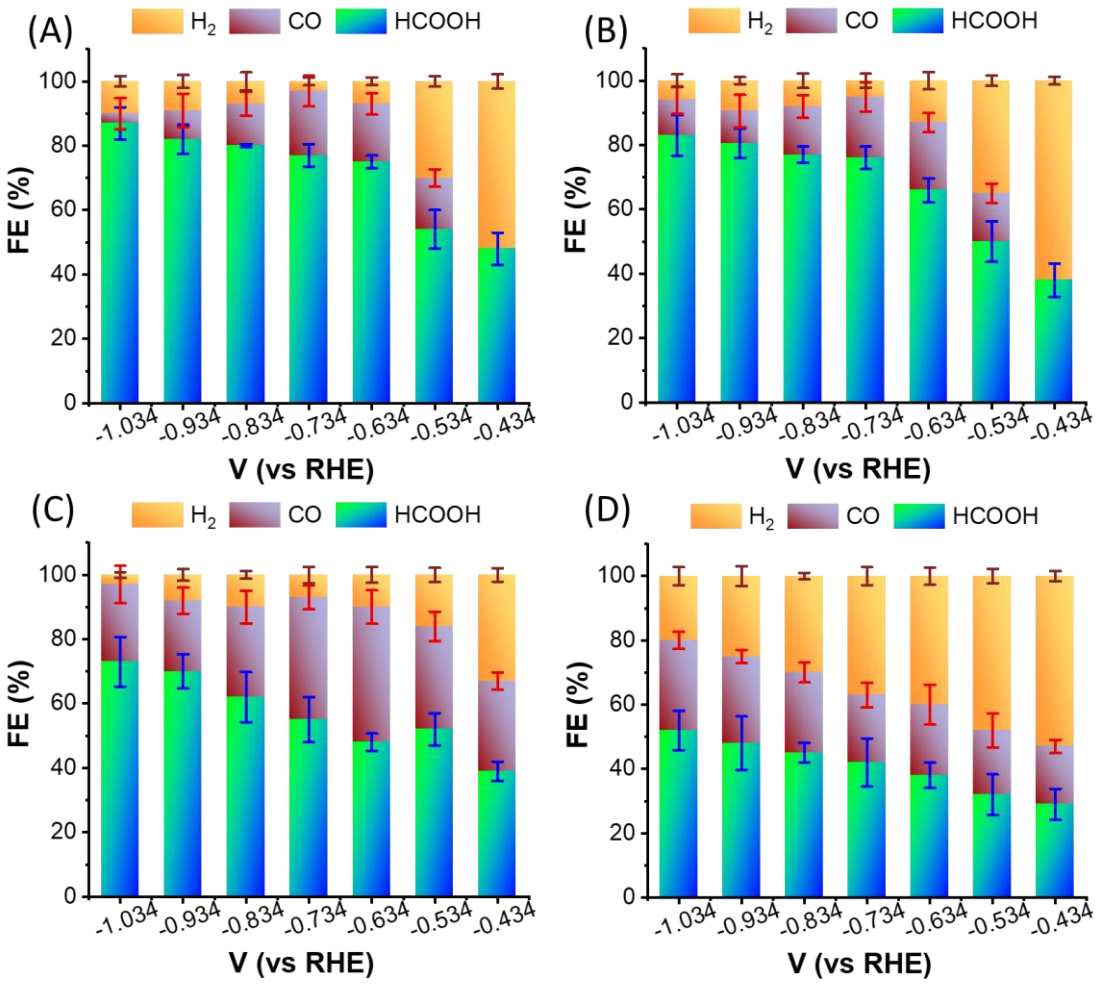

Fig. S9. FE of all products over (A) SnO_2 NF_CC, (B) SnO_2 NF_Sn Foil, (C) SnO_2 QD, (D) Bare Sn Foil.

Table S1. Comparison of the Sn – based CO_2RR electrocatalysts for formate production

Catalysts	Potential (vs RHE) @ current density	Electrolyte	Durability	FE_{HCOO^-}	Cell Type	Ref.
SnO_2 NF	**-1.2 V @ 45 mA cm^{-2}**	**0.5 M $NaHCO_3$**	**24 h**	**~90%**	**3-electrode H-type Cell**	**This Work**
P-Sn/SnO_x	-0.97 V @ 315.0 mA cm^{-2}	1.0 M KOH	120 h	90 %	GDE Flow Cell	[10]
π-SnS	-1.5 V @ 730 mA cm^{-2}	0.5 M K_2SO_4+H_2SO_4	12 h	92.15 %	GDE Flow Cell	[11]
Sn-Cu/SnOx	-0.7 V @ 406.7 mA cm^{-2}	1.0 M KOH	40 h	94 %	GDE Flow Cell	[12]
Bi_1-O-Sn_1@C	-1.5 V @ 310 mA cm^{-2}	1.0 m $KHCO_3$	5 h	93 %	Flow Cell	[13]
SnO/Cu_xO/CF/ CDL	-1.2 V @ 1152 mA cm^{-2}	1.0 M KOH	20 h	99 %	Flow Cell	[14]
Cu-SnO_2	-0.8 V @ 500 mA cm^{-2}	1.0 M KOH	50 min	91%	GDE Flow Cell	[15]
Cu_6Sn_5	-1.8 V @ 1500 mA cm^{-2}	3 M KCl +0.05 M H_2SO_4	300 h	91%	Flow Cell	[16]
Sn(S)/Au	-0.75 V @ 55 mA cm^{-2}	0.1 M $KHCO_3$	-	93.3%	3 – electrode undivided Cell	[17]
AgSn/SnO_x	-0.8 V @ 16 mA cm^{-2}	0.5 M $KHCO_3$	25 h	80 %	3 – electrode H – type Cell	[18]
$Sn_{56.3}Pb_{43.7}$	-2.0 V (vs Ag/AgCl) @ 45.7 mA cm^{-2}	0.5 M $KHCO_3$	2 h	79.8 %	3 – electrode H – type Cell	[19]

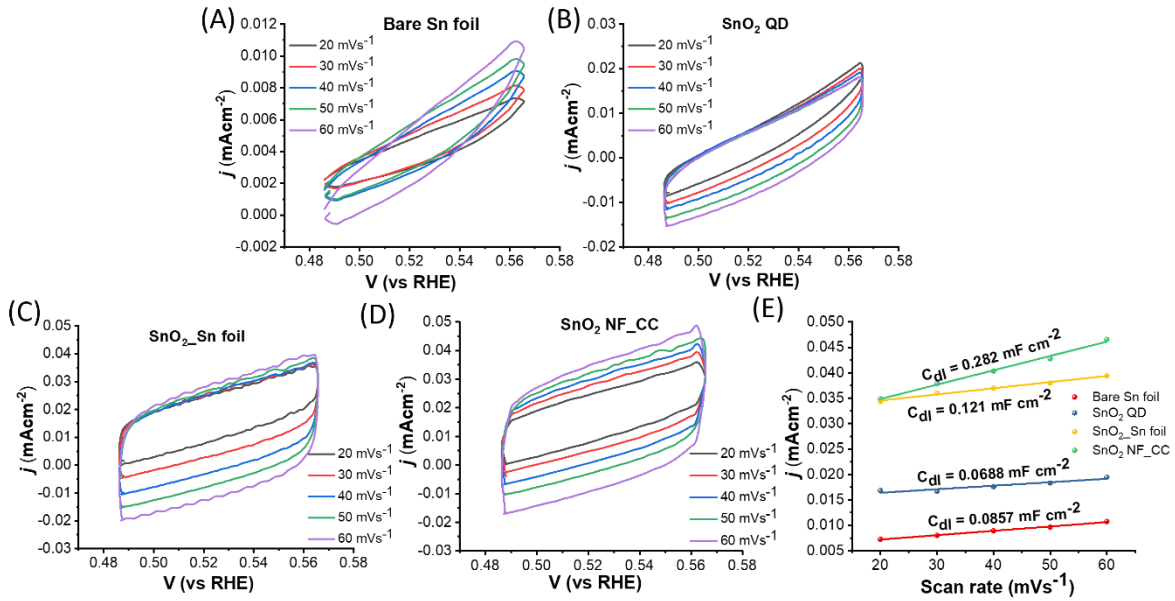

Fig. S10. Cyclic voltammograms (CVs) in non-Faradaic region of catalysis at scan rate of 20, 30, 40, 50 and 60 mVs^{-1} in CO_2 saturated 0.5 M $NaHCO_3$ solution of (A) bare Sn-foil, (B) SnO_2 QDs, (C) SnO_2 NF over Sn foil and (D) SnO_2 NF deposited over carbon cloth. (E) The linear fit of $\frac{\Delta j}{2}$ vs scan rate plot of all the catalysts. The slopes give double layer capacitance (C_{dl}) values of corresponding catalysts. The following equation was used to derive the ECSA values form C_{dl} values: ECSA= $\frac{C_{dl}}{0.04}$

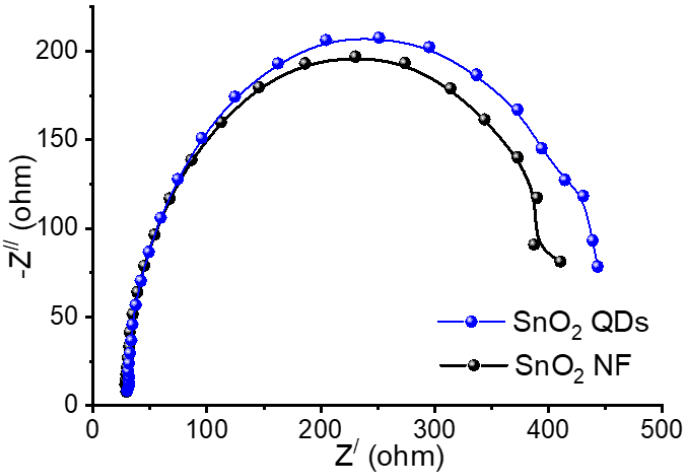

Fig. S11. Nyquist plots of the SnO_2 QDs and NFs at a potential of -1.6 V vs Ag/AgCl in CO_2 saturated 0.5 M $NaHCO_3$ solution.

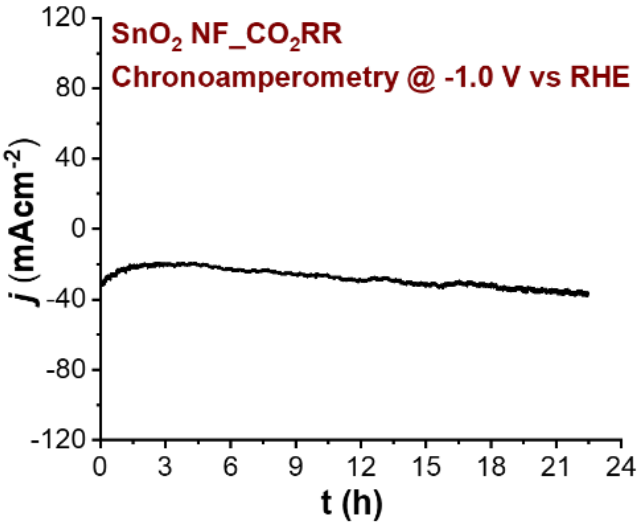

Fig. S12. Chronoamperometry curve of SnO_2 NF deposited over CC for 22h at -1.0 V vs RHE potential in presence of continues CO_2 purging.

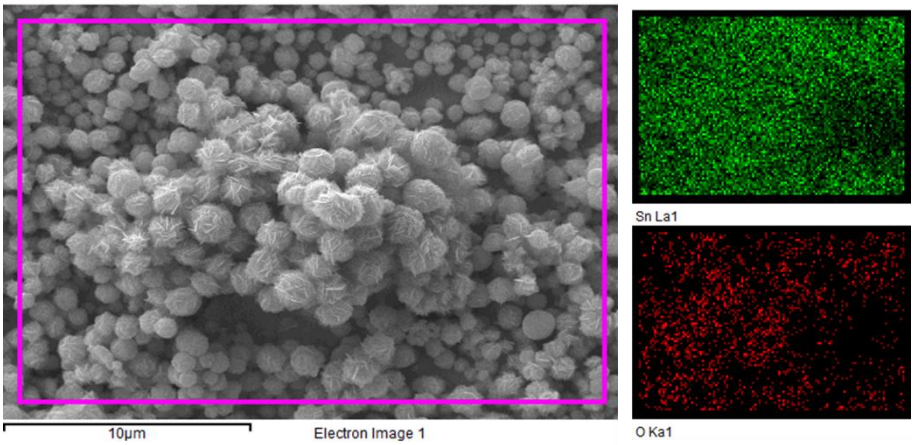

Fig. S13. SEM image and corresponding element mapping showing some degradation of flower morphology after 22 h of electrolysis.

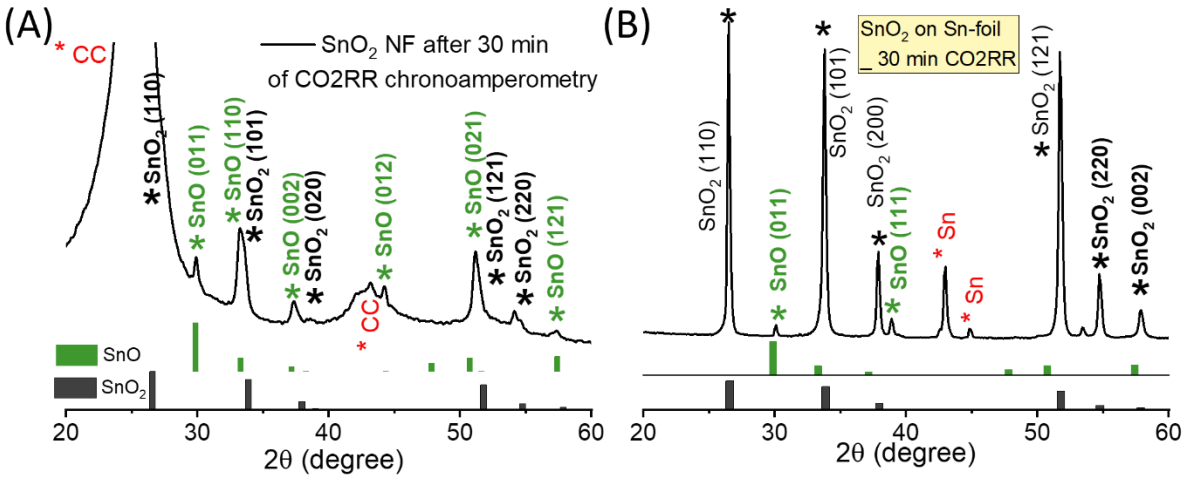

Fig. S14: XRD pattern of (A) SnO_2 NF deposited over carbon cloth and (B) SnO_2 NF grown over Sn-foil after 30 m of chronoamperometry study in CO_2RR condition.

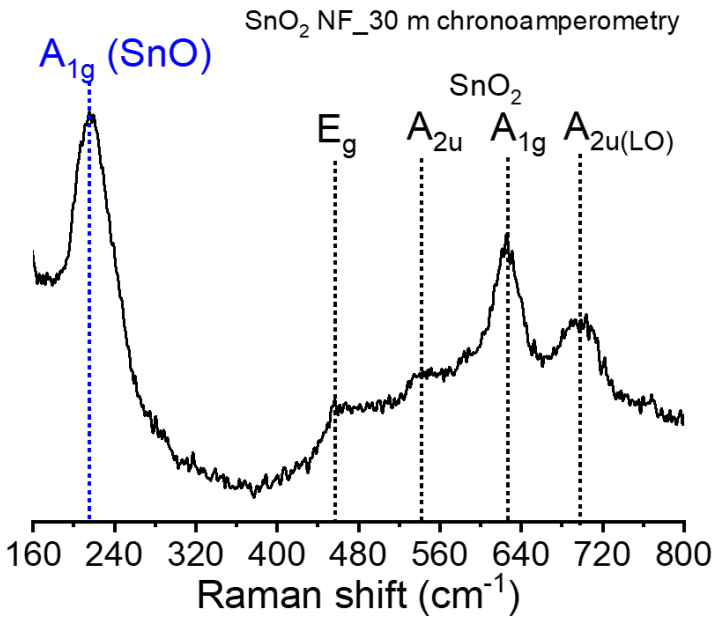

Fig. S15. Raman spectrum of SnO_2 NF after 30 m chronoamperometry study in CO_2RR condition.

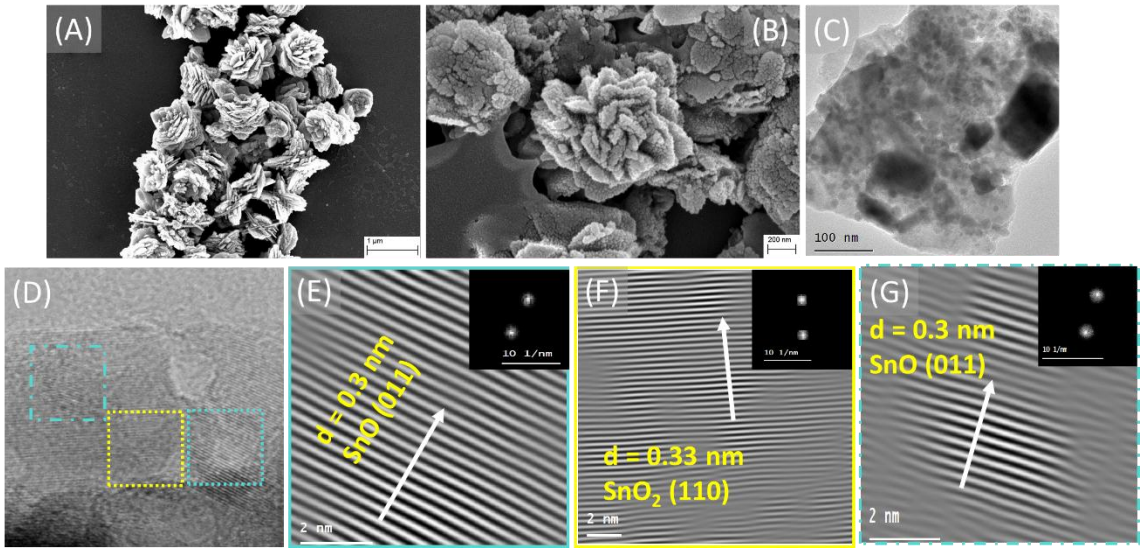

Fig. S16: SEM image of (A) SnO_2 nanoflowers and (B) a single nanoflower after 30 min of chronoamperometry study. (C) TEM image of a single nano-petal shows polycrystallinity with formation of multiple grain boundary. (D) HRTEM image of corner of single nanopetal. (E) HRTEM image with corresponding FFT from cyan squared area in Fig. (D) showing presence of (011) plane of SnO. (F) HRTEM image with FFT from yellow squared area in Fig. (D) showing presence of (110) plane of SnO_2. (G) HRTEM image with FFT from dashed cyan square area in Fig. (D) showing the presence of (011) plane of SnO.

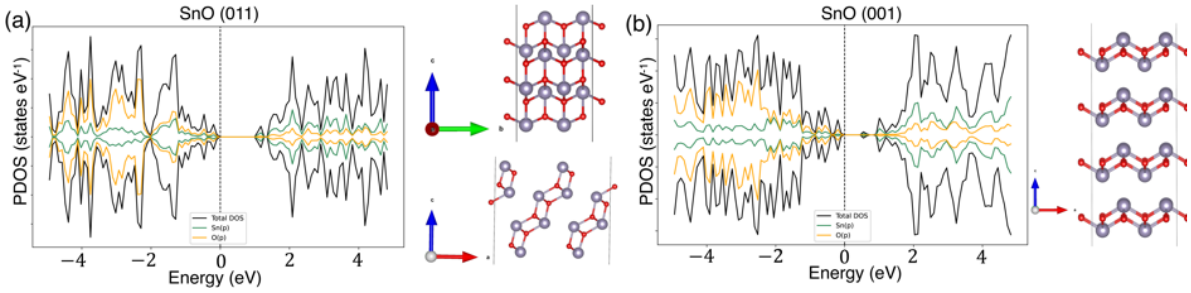

Fig. S17: Partial density of states of a) SnO (011) b) SnO (001) and their optimized surface.

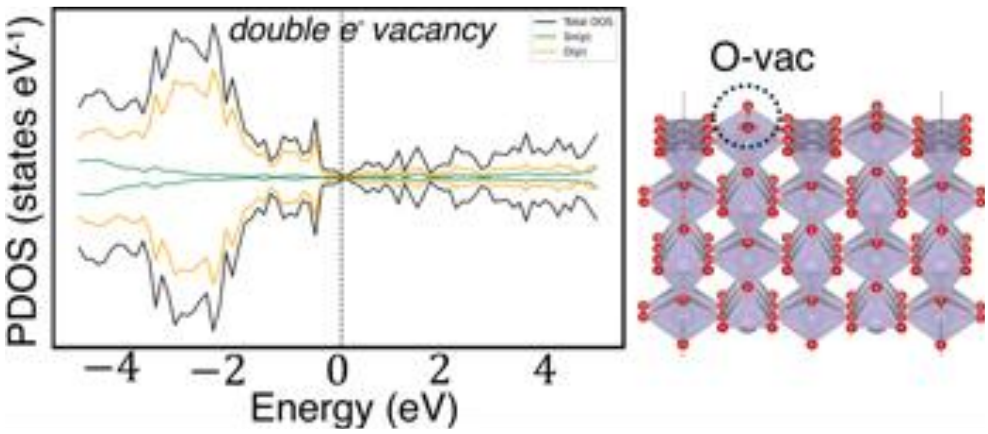

Fig. S18: Partial density of states of SnO_2 with O-vacancy (double electrons), and their optimized surface.

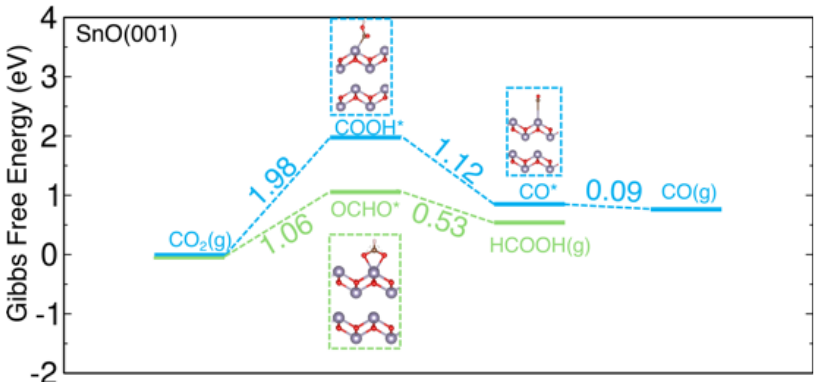

Fig. S19: Gibbs free energy profile for SnO (001) surface for CO_2 reduction reaction.

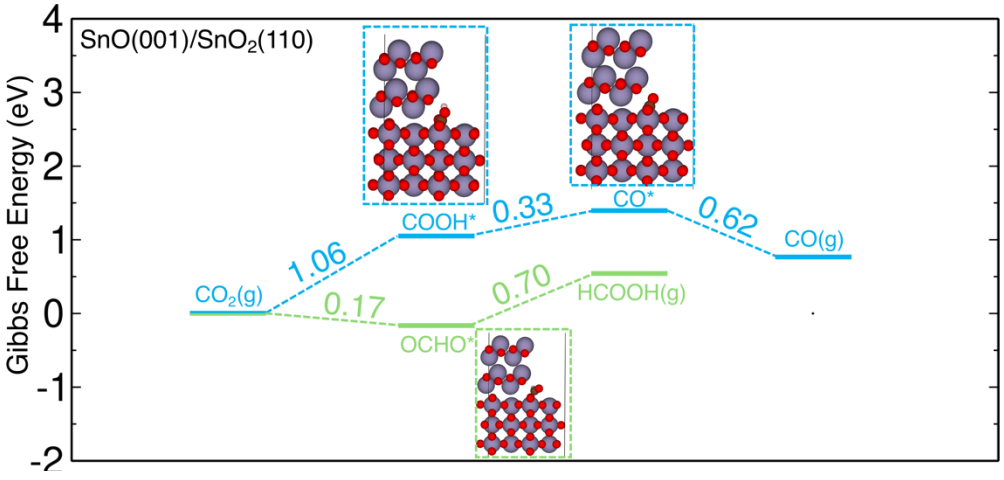

Fig. S20: Gibbs free energy profile for SnO(001)/SnO_2(110) surface for CO_2 reduction reaction.

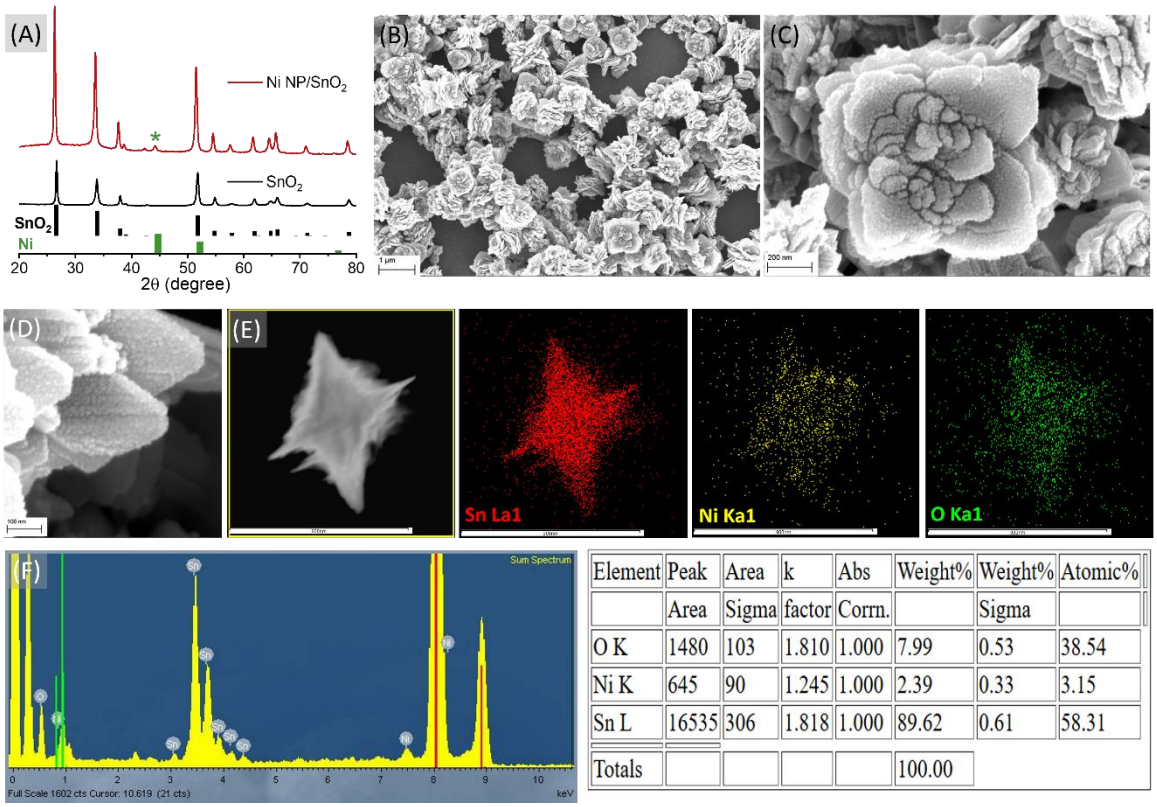

Element	Peak Area	Area Sigma	k factor	Abs Corrn.	Weight%	Weight% Sigma	Atomic%
O K	1480	103	1.810	1.000	7.99	0.53	38.54
Ni K	645	90	1.245	1.000	2.39	0.33	3.15
Sn L	16535	306	1.818	1.000	89.62	0.61	58.31
Totals					100.00		

Fig. S21. (A) XRD pattern of Ni–SnO_2 heterostructures showing diffraction peaks corresponding to both Ni and SnO_2. (B) SEM image of Ni-decorated SnO_2 nanoflowers on Sn foil. (C) SEM image of a single nanoflower, and (D) magnified view of nanopetals, confirming the presence of Ni on SnO_2. (E) STEM image of an individual nanoflower with corresponding elemental maps of Sn, Ni, and O. (F) EDS spectrum revealing the presence of Ni in the nanoflowers, with an atomic percentage of 3.15%.

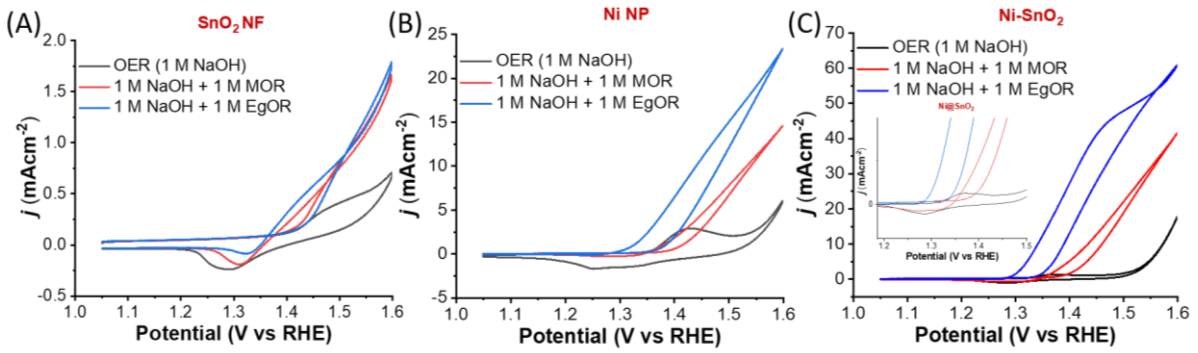

Fig. S22. Electrocatalytic oxidation activity (CV curves) for (A) SnO_2 NFs, (B) Ni nanoparticles NPs, and (C) Ni–SnO_2 heterostructures toward water oxidation (OER), methanol oxidation (MOR), and ethylene glycol oxidation (EgOR) in 1 M NaOH. The inset in (C) highlights the overlap of MOR and EgOR onset potentials with the $Ni^{2+} \rightarrow Ni^{3+}$ redox peak.

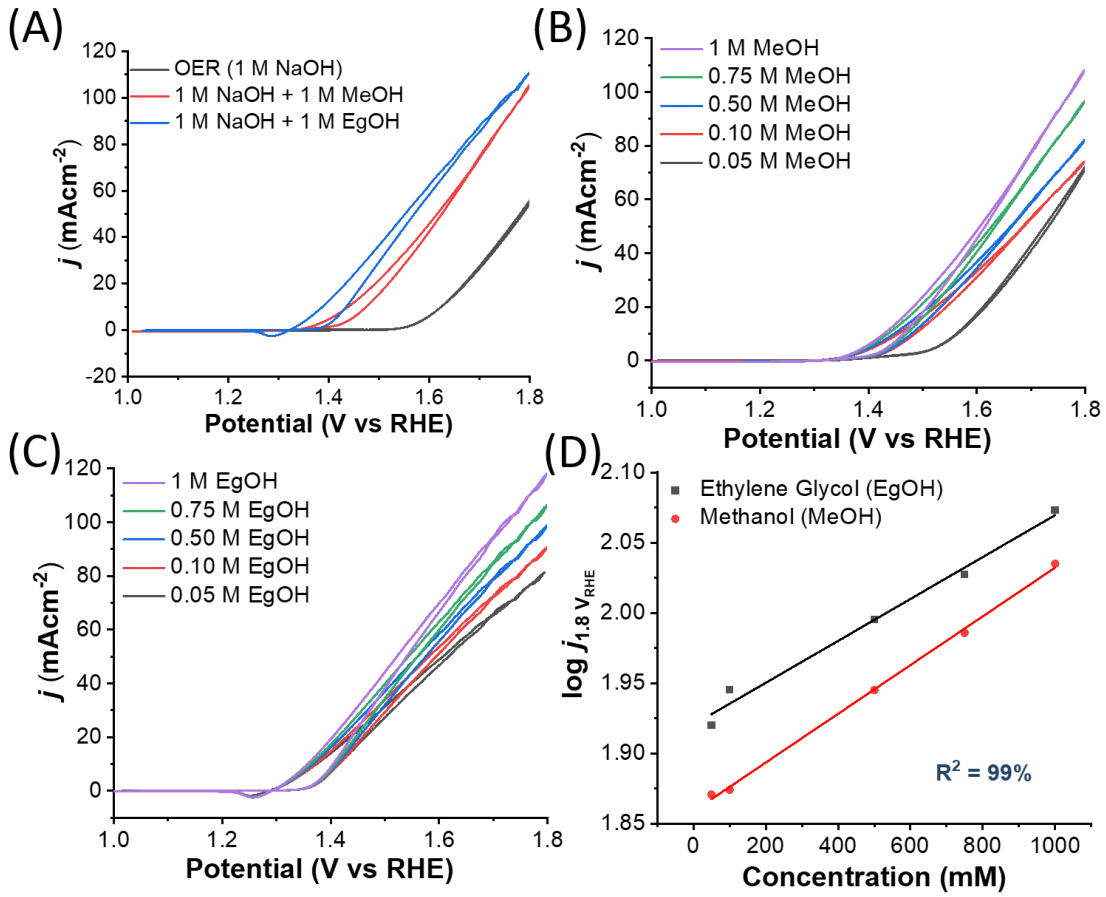

Fig. S23. (A) CV curves of Ni–SnO_2 NFs in 1 M NaOH, 1 M NaOH + 1 M CH_3OH, and 1 M NaOH + 1 M ethylene glycol. (B) CV profiles of Ni–SnO_2 NFs at a scan rate of 10 mVs^{-1} in 1 M NaOH with (B) varying methanol concentrations and (C) varying ethylene glycol concentrations. (D) Logarithmic current density (log *j*) versus concentration plot for methanol and ethylene glycol oxidation on the Ni–SnO_2 anode.

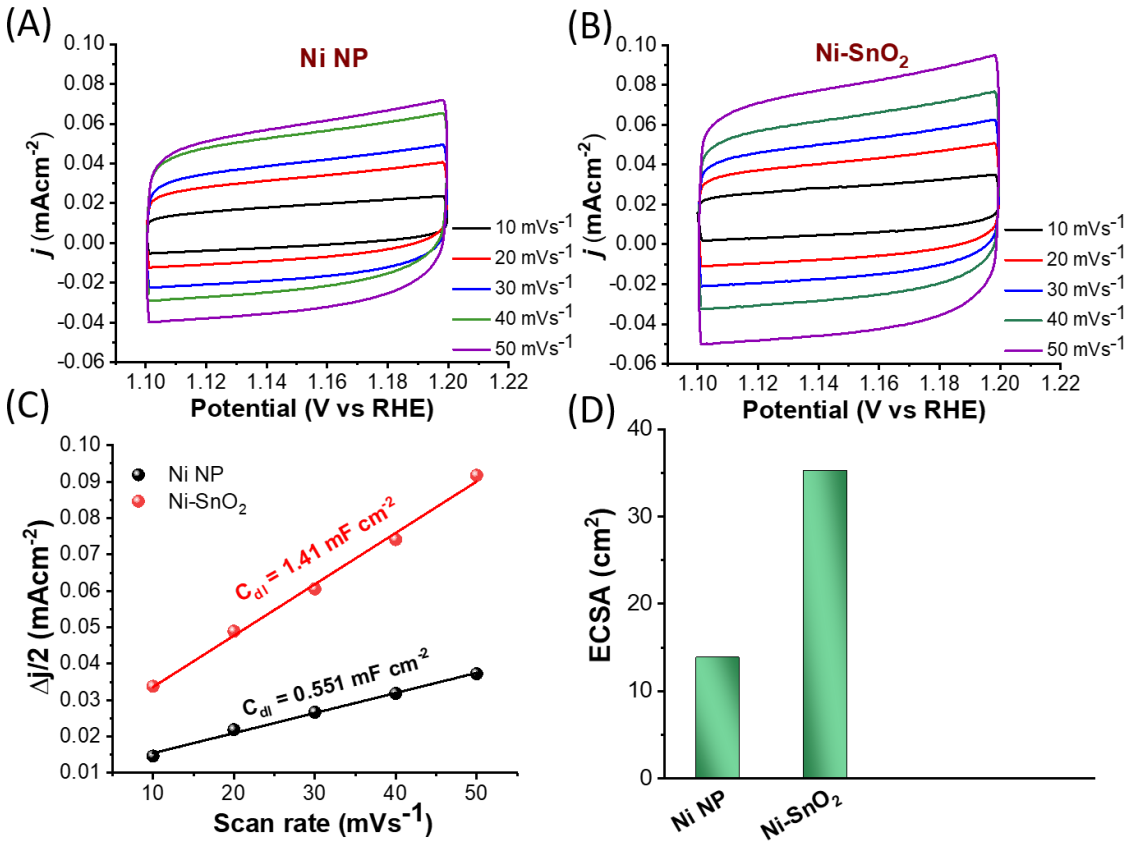

Fig. S24. (A, B) CV curves at varying scan rates in the non-Faradaic region for (A) Ni NPs and (B) the Ni–SnO_2 heterostructure. (C) Linear fitting of the Δj (anodic vs. cathodic current difference) versus scan rate to determine the double-layer capacitance (C_{dl}). (D) Comparative bar plots of the electrochemical active surface area (ECSA) values.

Table S2. Charge redistribution before and after adsorption for methanol and ethylene glycol on Ni, SnO_2, and Ni-SnO_2 surfaces.

System	O (ΔQ)	H (OH) (ΔQ)	C (ΔQ)	Other H (ΔQ)	Surface Metal ΔQ
Methanol on Ni	-1.25 – (–1.10) = –0.15 e	0.70 – 0.59 = +0.11 e	0.19 – 0.37 = –0.18 e	+0.05 to +0.10 e each	Ni: ~–0.01 to –0.02 e
Ethylene Glycol on Ni	-1.36 – (–1.15) = –0.21 e; -1.23 – (–1.10) = –0.13 e	0.83 – 0.61 = +0.22 e; 0.67 – 0.58 = +0.09 e	0.33/0.35 – 0.46/0.44 = ~–0.11 e avg	+0.02 to +0.07 e each	Ni: ~–0.03 e
Methanol on SnO_2	-1.17 – (–1.10) = –0.07 e	0.57 – 0.59 = –0.02 e	0.07 – 0.37 = –0.30 e	0.12, 0.18, 0.24 – 0.04–0.06 = ~+0.10 to +0.20 e each	Sn: 2.04, 2.14 – 2.10 = ~–0.06, +0.04 e
Ethylene Glycol on SnO_2	-1.15 – (–1.15) = 0 e; -0.95 – (–1.10) = +0.15 e	0.71 – 0.61 = +0.10 e; 0.64 – 0.58 = +0.06 e	0.32/0.34 – 0.46/0.44 = ~–0.12 e avg	+0.02 to +0.06 e each	Sn: +0.13 and +0.08 e
Methanol on Ni (Ni/SnO_2)	-1.25 – (–1.10) = –0.15 e	0.75 – 0.59 = +0.16 e	0.17 – 0.37 = –0.20 e	+0.05 to +0.10 e each	Ni: 0.03 → 0.17 = +0.14 e lost
Ethylene Glycol on Ni (Ni/SnO_2)	-1.26 – (–1.15) = –0.11 e; -1.23 – (–1.10) = –0.13 e	0.74 – 0.61 = +0.13 e; 0.69 – 0.58 = +0.11 e	0.32/0.34 – 0.46/0.44 = ~–0.12 e avg	+0.02 to +0.08 e each	Ni: 0.03 → 0.19 and 0.10 = ~+0.16 e lost

Bader charge analysis reveals distinct charge redistribution patterns for methanol and ethylene glycol adsorbed on Ni, SnO_2, and Ni-SnO_2 surfaces. On pure Ni, methanol adsorption leads to a charge gain of ~0.15 e on the oxygen atom, with nearby Ni atoms donating a modest ~0.01–0.02 e. Ethylene glycol binds more strongly via both hydroxyl groups, with the two oxygen atoms gaining a total of ~0.34 e and the Ni surface donating ~0.03 e, consistent with a bidentate interaction. On SnO_2, methanol shows minimal charge redistribution, while ethylene glycol transfers ~0.15 e from one oxygen atom to the surface, and nearby Sn atoms gain a total of ~0.2 e. In contrast, the Ni-SnO_2 heterostructure exhibits enhanced interfacial charge transfer. When methanol is adsorbed, the oxygen atom gains ~0.15 e and Ni atoms at the interface lose ~0.14 e. For ethylene glycol, the two oxygen atoms gain ~0.24 e in total, while interfacial Ni atoms donate ~0.16 e. Although the net charge gain on ethylene glycol is slightly lower than on pure Ni, the significantly higher electron donation from Ni-SnO_2 indicates stronger electronic activation at the interface. These results support the DFT-calculated adsorption energies and highlight the synergistic effect of the oxide support in modulating surface reactivity.

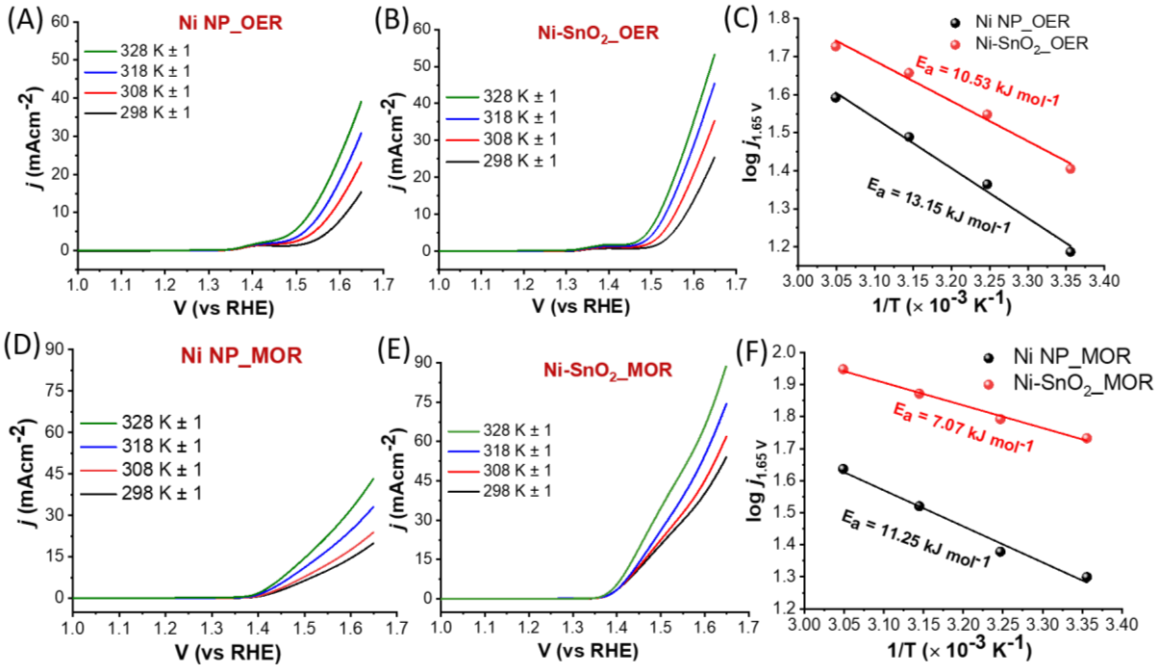

Fig. S25. Linear sweep voltammetry (LSV) curves recorded at various temperatures for (A) Ni nanoparticles (Ni NP) and (B) Ni–SnO_2 heterostructure in 1 M NaOH at a scan rate of 10 mVs^{-1} for the oxygen evolution reaction (OER). (C) Corresponding Arrhenius plots (log *j* vs. 1/T) for the OER activity of the catalysts. LSV curves obtained at different temperatures for (D) Ni NP and (E) Ni–SnO_2 heterostructure in 1 M NaOH at a scan rate of 10 mVs^{-1} for the methanol electrooxidation reaction (MOR). (F) Corresponding Arrhenius plots (log *j* vs. 1/T) for MOR performance.

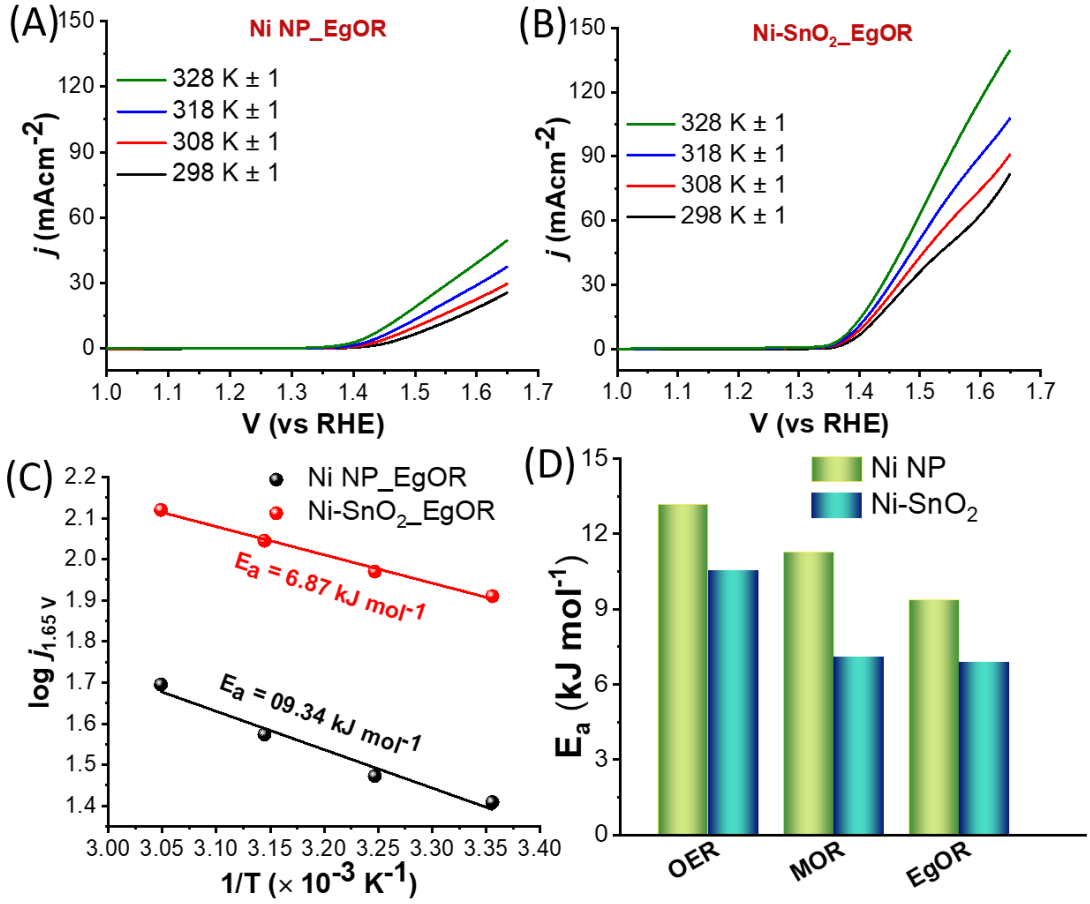

Fig. S26. LSV curves at different temperatures for (A) Ni NP and (B) Ni-SnO_2 heterostructure in 1M NaOH at a scan rate of 10 mVs^{-1} for EgOR. (C) The corresponding Arrhenius comparison plot (log *j* Vs 1/T) of the catalysts. (D) Comparative activation energy plots of OER, MOR and EgOR.

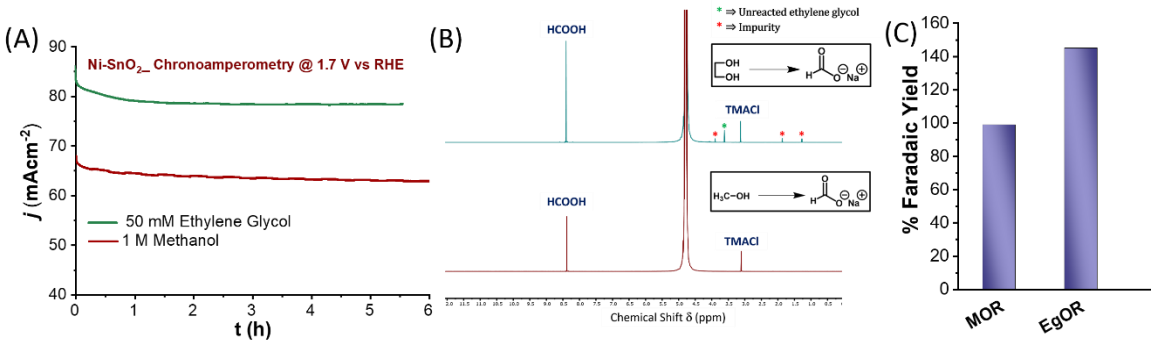

Fig. S27. (A) Chronoamperometry curves recorded during bulk electrolysis of ethylene glycol oxidation (EgOR) and methanol oxidation (MOR) in 6 mL of 1 M NaOH containing 50 mM ethylene glycol and 1 M methanol, respectively, at 1.7 V vs. RHE using the Ni–SnO_2 electrocatalyst. (B) ^{1}H NMR spectra (500 MHz, D_2O-locked) of the post-electrolysis solution, showing the formation of formic acid from both ethylene glycol and methanol. (C) Faradaic yield (%) of formic acid produced via MOR and EgOR at high current density.

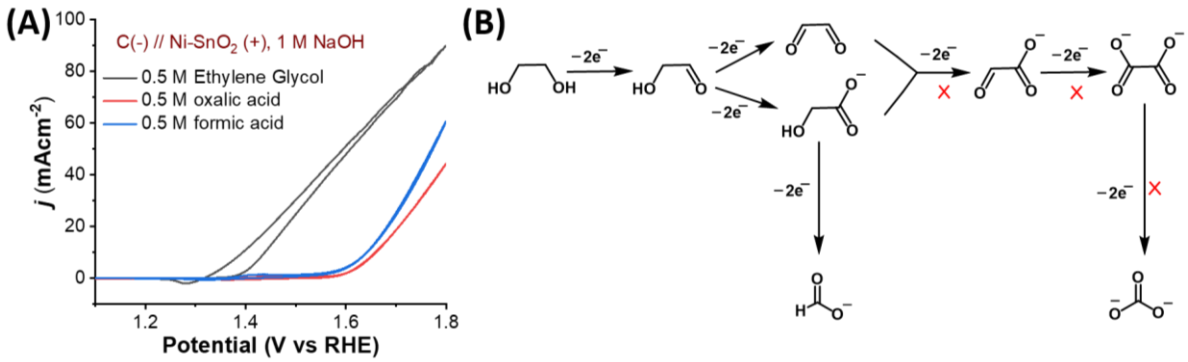

Fig. S28. (A) Cyclic voltammetry (CV) curves showing the electro-oxidation of ethylene glycol (EgOR), oxalic acid, and formic acid using Ni–SnO_2 as the anode electrocatalyst. (B) Proposed reaction pathways derived from the CV data presented in panel (A).

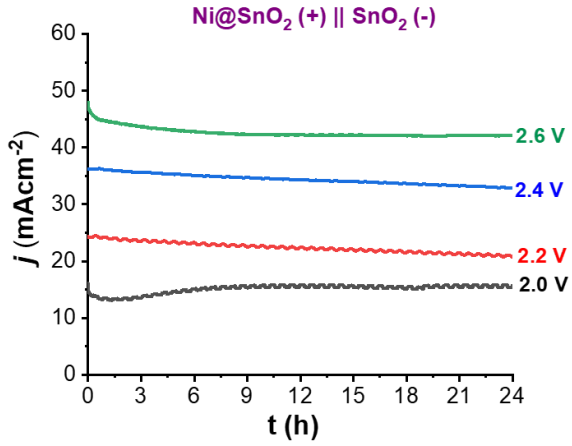

Fig. S29. Chronoamperometric curves recorded during bulk hybrid CO_2RR electrolysis coupled with EgOR at various applied potentials.

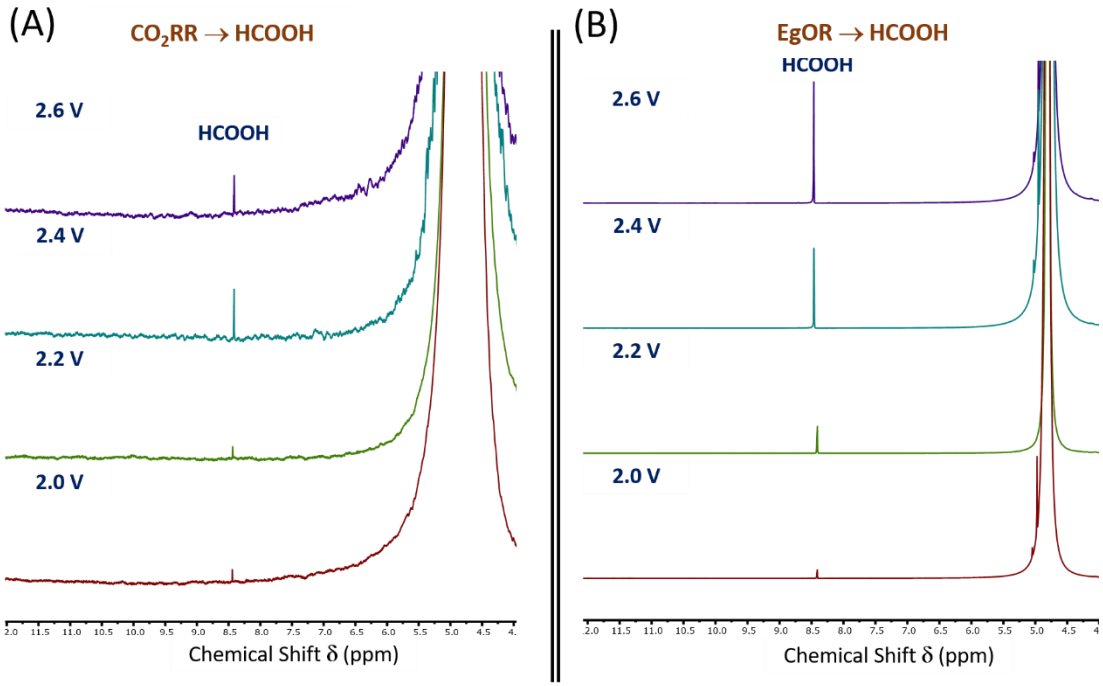

Fig. S30. ^{1}H NMR spectra of the post electrolytic solution of hybrid CO_2RR where cathode reaction was CO_2RR and anode reaction EgOR. The NMR spectra show the formation of formic acid both from cathodic (A) and anodic (B) reaction when bulk electrolysis were performed at four different potentials.

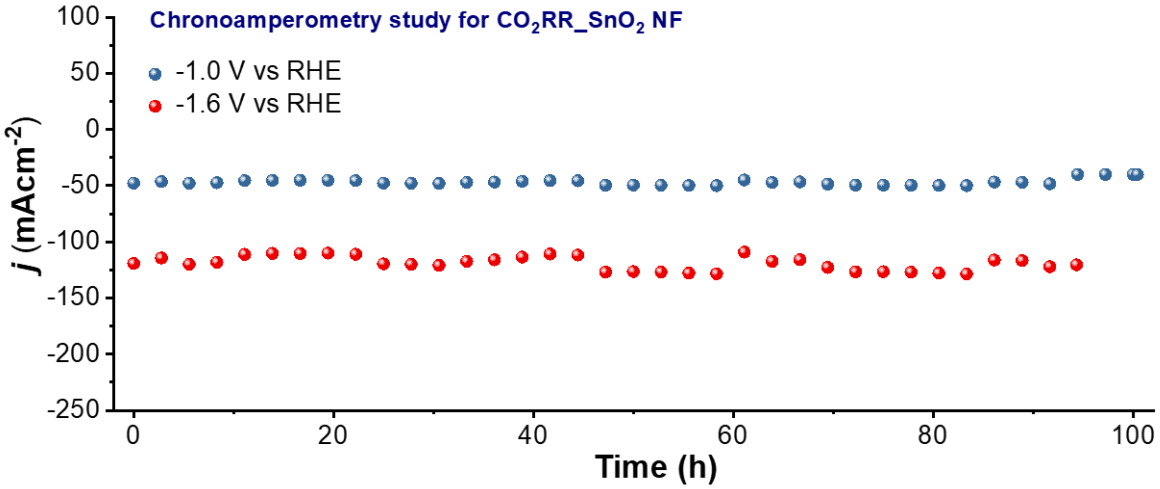

Fig. S31. Chronoamperometry plot at different potential for $CO_2RR||OER$ system with SnO_2 NF in a GDL based flow cell electrolyzer for 100h.

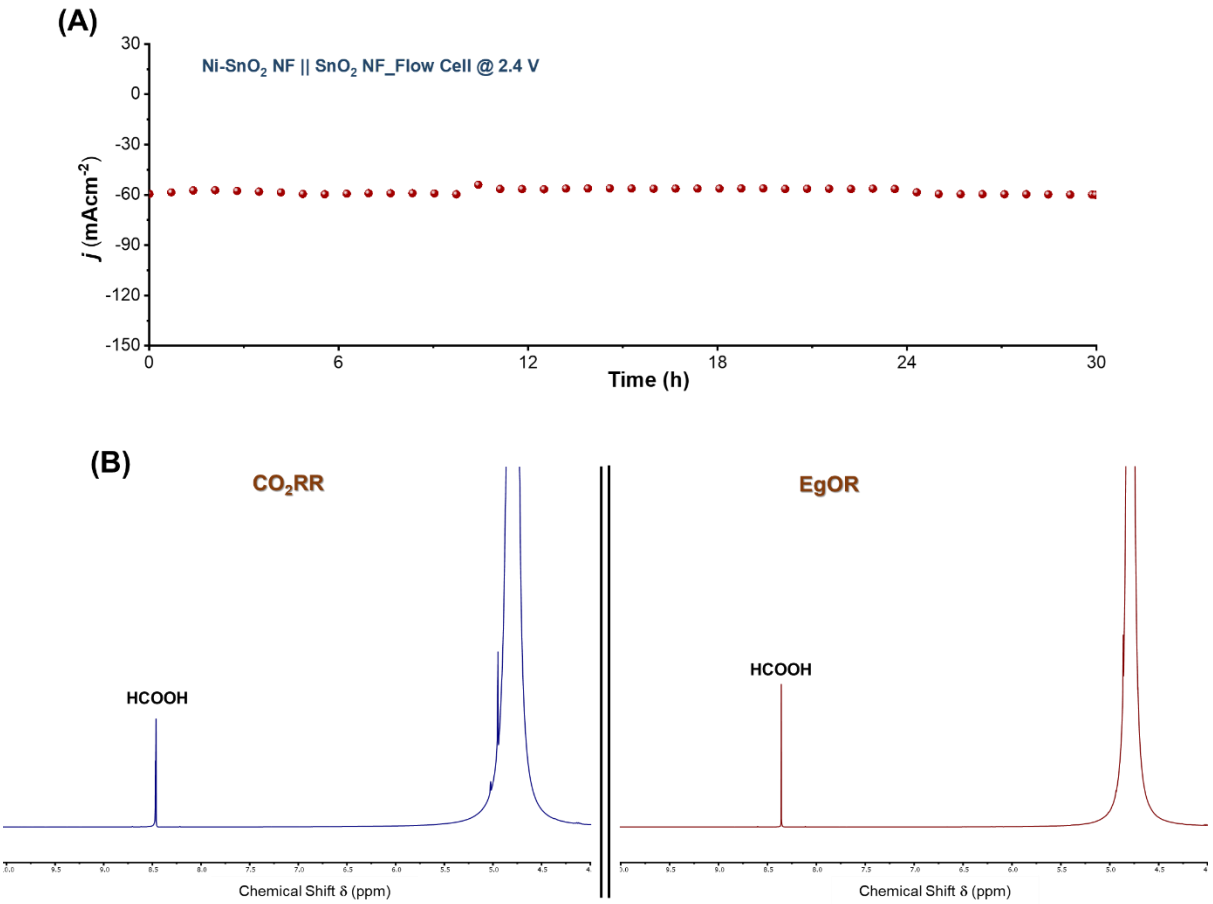

Fig. S32. (A) Chronoamperometric plot of the hybrid CO2RR||EgOR system in a flow cell configuration at 2.4 V. (B) ^{1}H NMR spectra of the post catholyte and anolyte solutions (from left to right) of hybrid CO_2RR flow cell.

Table:3. Comparison of the electrocatalysts for the coproduction of formate from paired CO_2RR- MOR, EgOR electrolysis.

Cell Configuration Anode (+) || Cathode (-)	Cell Type	Anodic reaction/ Product	Cathodic reaction/ Product	Cell Potential @ current density	Potential Advantage compared to OER || CO_2RR	FE_{HCOO^-} (Anode / Cathode)	Ref.
Ni-SnO_2 NF || SnO_2 NF	**H-type Cell**	**EgOH/ Formate**	**CO_2RR/ Formate**	**2.083 V @ 20 mA cm^{-2}**	**430 mV @ 10 mA cm^{-2}**	**93 % / 85 %**	**This Work**
Ni-SnO_2 NF || SnO_2 NF	**GDE Flow Cell**	**EgOH/ Formate**	**CO_2RR/ Formate**	**1.91 V @ 20 mA cm^{-2}**	**480 mV @ 20 mA cm^{-2}**	**95 % / 88 %**	**This Work**
$NiCo_2O_4$ || SnO_2	Homemade H- type electrolyzer	PET-derived EgOH/ Formate	CO_2RR/ Formate	1.9 V @ 20 mA cm^{-2}	180 mV @ 20 mA cm^{-2}	90 % / 82 %	20
$Ni(OH)_2 – V_O$ || Bi/Bi_2O_3	Solar driven flow reactor	PET-derived EgOH/ Formate	CO_2RR/ Formate	2.7 V @ 100 mA cm^{-2}	-	86 % / 91 %	21
CuCoO@rGO || BOC@rGO	H-type Cell	PET-derived EgOH/ Formate	CO_2RR/ Formate	1.9 V @ 10 mA cm^{-2}	230 mV @ 10 mA cm^{-2}	85.5 % / 97.4 %	22
Cu(F)@CuO@$Ni(OH)_2$ || Cu(F)@Pd-SnO	H-type Cell	EgOH/ Formate	CO_2RR/ Formate	1.63 V @ 10 mA cm^{-2}	180 mV @ 10 mA cm^{-2}	75 % / 89 %	23
$NiCo_2O_4$-NF || BiOI-C	MEA electrolyzer	PET-derived EgOH/ Formate	CO_2RR/ Formate	2.7 V @ 250 mA cm^{-2}	240 mV @ 30 mA cm^{-2}	90 % / 92.3 %	24
Au/$Ni(OH)_2$ || Bi	MEA electrolyzer	PET-derived EgOH/ Formate	CO_2RR/ Formate	2.18 V @ 100 mA cm^{-2}	-	98 % / 90 %	25
Vo-BOC-NS||Ni_3N-Co_3N	Flow Cell	MeOH/ Formate	CO_2RR/ Formate	2.27 V @ 50 mA cm^{-2}	-	100 % / 90 %	26
Bi_2O_3-SnO@CuO|| Bi_2O_3-SnO@CuO	H-type Cell	MeOH/ Formate	CO_2RR/ Formate	1.45 V @ 30 mA cm^{-2}	>200 mV @ 10 mA cm^{-2}	97.5 % / 94.7 %	27
CuSn||CuSn	H-type Cell	MeOH/ Formate	CO_2RR/ Formate	3.23 V @ 100 mA cm^{-2}	610 mV @ 100 mA cm^{-2}	99.9 % / 87.3 %	28
Ni-BDC/NF || Bi-BDC/GDL	Flow Cell	MeOH/ Formate	CO_2RR/ Formate	3.23 V @ 100 mA cm^{-2}	430 mV @ 10 mA cm^{-2}	95 % / 94 %	29
Mn/CoOOH || Ov-rich BOC	Flow Cell	EgOH/ Formate	CO_2RR/ Formate	2.2 V @ 150 mA cm^{-2}	-	94.2 % / 95.3 %	30
3D Ni foam || Bi_2CO_3	Flow Cell	EgOH/ Formate	CO_2RR/ Formate	2.91 V @ 1 A cm^{-2}	-	93.7 % / 86 %	31
$NiOOH_5$/NF || Bi_2CO_3	Flow Cell	EgOH/ Formate	CO_2RR/ Formate	~2.45 V @ 100 A cm^{-2}	-	90 % / 70 %	32
Mo-Ni_2P/NF || RC-Bi/CP	Flow Cell	EgOH/ Formate	CO_2RR/ Formate	~2.0 V @ 100 A cm^{-2}	259 mV @ 100 mA cm^{-2}	94 % / 92 %	33

References

1. S. Ghosh, K. Das, K. Chakrabarti and S. K. De, *CrystEngComm*, 2012, **14**, 929-935.
2. S. Ghosh, K. Das, K. Chakrabarti and S. K. De, *Dalton Trans.*, 2013, **42**, 3434-3446.
3. J. P. Perdew and Y. Wang, *Phys. Rev. B*, 1992, **45**, 13244-13249.
4. J. P. Perdew, K. Burke and M. Ernzerhof, *Phys. Rev. Lett.*, 1996, **77**, 3865-3868.
5. M. Karamad, H. A. Hansen, J. Rossmeisl and J. K. Nørskov, *ACS Catal.*, 2015, **5**, 4075-4081.
6. M. Chase, *Journal*, 1998.
7. L. Wang, T. Maxisch and G. Ceder, *Phys. Rev. B*, 2006, **73**, 195107.
8. Z. Zeng, M. K. Y. Chan, Z.-J. Zhao, J. Kubal, D. Fan and J. Greeley, *J. Phys. Chem. C*, 2015, **119**, 18177-18187.
9. J. K. Nørskov, J. Rossmeisl, A. Logadottir, L. Lindqvist, J. R. Kitchin, T. Bligaard and H. Jónsson, *J. Phys. Chem. B*, 2004, **108**, 17886-17892.
10. C. Cheng, T. Liu, Y. Wang, P. Wei, J. Sang, J. Shao, Y. Song, Y. Zang, D. Gao and G. Wang, *J. Energy Chem.*, 2023, **81**, 125-131.
11. H. Shen, H. Jin, H. Li, H. Wang, J. Duan, Y. Jiao and S.-Z. Qiao, *Nat Commun* 2023, **14**, 2843.
12. K. Ye, Z. Zhou, J. Shao, L. Lin, D. Gao, N. Ta, R. Si, G. Wang and X. Bao, *Angew. Chem. Int. Ed.*, 2020, **59**, 4814-4821.
13. N. Wang, C. Shao, R. Zhang, Y. Zhang, Z. Min, B. Chang, M. Fan and J. Wang, *Small*, 2024, **20**, 2306129.
14. T. Liu, K. Ohashi, K. Nagita, T. Harada, S. Nakanishi and K. Kamiya, *Small* 2022, **18**, 2205323.
15. Y. Jiang, J. Shan, P. Wang, L. Huang, Y. Zheng and S.-Z. Qiao, *ACS Catal.* , 2023, **13**, 3101-3108.
16. X. Yu, Y. Xu, L. Li, M. Zhang, W. Qin, F. Che and M. Zhong, *Nat Commun*, 2024, **15**, 1711.
17. X. Zheng, P. De Luna, F. P. García de Arquer, B. Zhang, N. Becknell, M. B. Ross, Y. Li, M. N. Banis, Y. Li, M. Liu, O. Voznyy, C. T. Dinh, T. Zhuang, P. Stadler, Y. Cui, X. Du, P. Yang and E. H. Sargent, *Joule*, 2017, **1**, 794-805.
18. W. Luc, C. Collins, S. Wang, H. Xin, K. He, Y. Kang and F. Jiao, *J. Am. Chem. Soc.*, 2017, **139**, 1885-1893.
19. S. Y. Choi, S. K. Jeong, H. J. Kim, I.-H. Baek and K. T. Park, *ACS Sustainable Chem. Eng.*, 2016, **4**, 1311-1318.
20. J. Wang, X. Li, M. Wang, T. Zhang, X. Chai, J. Lu, T. Wang, Y. Zhao and D. Ma, *ACS Catal.* , 2022, **12**, 6722-6728.
21. F. Ma, Z. Li, R. Hu, Z. Wang, J. Wang, J. Li, Y. Nie, Z. Zheng and X. Jiang, *ACS Catal.*, 2023, **13**, 14163-14172.
22. S. K. Kilaparthi, A. Addad, A. Barras, S. Szunerits and R. Boukherroub, *J. Mater. Chem. A,*, 2023, **11**, 26075-26085.
23. I. Bashir, J. D. McGettrick, M. F. Kühnel, B. Sarfraz, S. N. Arshad and A. Rauf, *ACS Sustainable Chem. Eng.*, 2024, **12**, 4795-4802.
24. P.-F. Sui, M.-N. Zhu, M.-R. Gao, Y.-C. Wang, R. Feng, X. Wang, S. Liu and J.-L. Luo, *Appl. Catal. B-Environ*, 2025, **373**, 125355.
25. D. Du, F. Kang, S. Yang, B. Shao and J. Luo, *Sci. China Chem.*, 2024, **67**, 1539-1544.
26. D. Du, F. Kang, S. Yang, B. Shao and J. Luo, . *InfoMat.*, 2024, **67**, 1539-1544.
27. Z. Tang, Y. Wang, W. Qian, Z. Piao, H. Wang and Y. Zhang, *J. Colloid Interface Sci.*, 2023, **652**, 1653-1664.
28. Y. Li, C.-Z. Huo, H.-J. Wang, Z.-X. Ye, P.-P. Luo, X.-X. Cao and T.-B. Lu, *Nano Energy*, 2022, **98**, 107277.
29. P. K. Das, T. Gupta, K. Peramaiah and B. Mondal, *Small Struct.*, 2025, **n/a**, 2500223.
30. H. Liu, Z. Wang, Y. He, X. Hu and L. Liu, *Appl. Catal., B*, 2025, **361**, 124667.

31. X. Yu, H. Rabiee, A. Dutta, Y. Li, Z. Szakály, S. Vesztergom, L. Warmuth, A. Rieder and P. Broekmann, *J. Am. Chem. Soc.*, 2025, **147**, 41481-41491.
32. Y. Fang, C. Cai, H. Yamashita, X. Qian and Y. Zhao, *Catal. Today*, 2026, **462**, 115544.
33. L. Jiang, Y. Du, J. Ye, L. Yuan, X. Liu, W. Tian and J. Ji, *Appl. Catal., B*, 2026, **386**, 126372.